

Two-dimensional perovskite capping layer for stable and efficient tin-lead perovskite solar cells

Jin Yuan¹, Yuanzhi Jiang¹, Tingwei He¹, Guodong Shi¹, Zixiong Fan¹ & Mingjian Yuan^{1,2*}

¹Key Laboratory of Advanced Energy Materials Chemistry (Ministry of Education), College of Chemistry, Nankai University, Tianjin 300071, China;

²Renewable Energy Conversion and Storage Center, Nankai University, Tianjin 300071, China

Received November 1, 2018; accepted February 8, 2019; published online March 7, 2019

Mixed tin-lead iodide perovskites exhibit the characteristics of low toxicity and improved light harvesting ability up to near-infrared (NIR) spectral region, making them as an attractive alternative for traditional lead based perovskites. However, the performance of lead-based perovskites solar cells is still far inferior to their lead analogues owing to the unavoidable oxidation of Sn^{2+} to Sn^{4+} . Here we introduced two-dimensional (2D) perovskite on the top of three dimensional (3D) perovskite film as a capping layer to reduce the self-oxidation, and thus improved the device stability. 2D capping layer was then confirmed by X-ray diffraction (XRD) and X-ray photoelectron spectroscopy (XPS) analysis. The existence of the 2D protecting thin layer significantly reduce the spontaneous Sn^{2+} oxidation, thus improve the device performance and reduce the hysteresis. The phenomena could be ascribed to the improved charge extraction efficiency causing by prohibited nonradiative recombination. On top of this, the photovoltaic devices based on conventional-structure configuration were fabricated. Taking advantage of the 2D capping layer, 2D/3D hybrid perovskite photovoltaic devices achieve a open-circuit voltage (V_{oc}) of 0.77 V with short circuit current density (J_{sc}) of 26.60 mA cm^{-2} , delivering the best-performing power conversion efficiency of 15.5%. Moreover, the 2D/3D perovskite devices maintained 60% its initial efficiency after 40 h exposed in air (humidity around 30%, temperature 22 °C), while 3D perovskite-based devices completely failed.

two-dimensional perovskites, tin-lead perovskites, 2D/3D, stability

Citation: Yuan J, Jiang Y, He T, Shi G, Fan Z, Yuan M. Two-dimensional perovskite capping layer for stable and efficient tin-lead perovskite solar cells. *Sci China Chem*, 2019, 62: 629–636, <https://doi.org/10.1007/s11426-018-9436-1>

1 Introduction

Organic-inorganic hybrid halide perovskite materials have attracted intense attention due to their impressive optoelectronic properties [1–4]. The power conversion efficiency (PCE) of perovskite solar cells (PSCs) has been remarkably boosted from 3.8% to 23.3% [5,6]. In spite of these advanced achievements, the toxicity of lead raised the safety concerns on human health and the environment, which hindered their further large-scale commercial application. Recently, much attention has been paid on developing less toxic elementals,

such as tin (Sn^{2+}), germanium (Ge^{2+}), bismuth (Bi^{3+}), antimony (Sb^{3+}), copper (Cu^{2+}) and titanium (Ti^{4+}) based perovskites to replace traditional Pb^{2+} based perovskites [7–12]. Among them, Sn^{2+} possesses the most similar ionic radius compared to Pb^{2+} . Accordingly, Sn^{2+} substitution will not severely alter the resulting crystal lattice parameter in principle [7]. In addition, Sn-based perovskites exhibit lower bandgap compared to their Pb-based analogues, thus are able to harvest more phonons up to near-infrared (NIR) spectral region. By taking advantage of these intrinsic properties, it is reasonable to combine Pb^{2+} with Sn^{2+} to generate a Sn-Pb alloyed perovskites. The resulting optical and electrical properties of alloyed perovskites can be fine-tuned through

*Corresponding author (email: yuanmj@nankai.edu.cn)

adjusting the ratio of Sn/Pb [13–16]. However, the device performance of Sn-Pb alloyed PSCs still lag behind that of their Pb^{2+} analogues. In particular, the alloyed Pb-Sn PSCs exhibit poor device performance and terrible device stabilities when the Sn/Pb ratio is higher than 1. The reasons leading to the poor device performance could be ascribed to the following aspects: (1) Sn^{2+} is a metastable species, therefore is easily affected by the fabrication conditions. Thus the instantaneous oxidation of Sn^{2+} to Sn^{4+} results in high levels of self p-doping, which subsequently serves as a carrier recombination center during the device operation [17,18]. (2) The low formation energy of Sn^{4+} leading to high hole concentration and recombination loss of the charge carriers [19,20]. (3) Fast reaction speed between SnI_2 and organic ammonium salts increases the difficulty in fabricating compact and pinhole free perovskite films via one-step antisolvent assisted deposition method.

Important progress has been made to meet these challenges. Dimethyl-sulfoxide (DMSO) utilized in perovskite precursor solution was demonstrated to be important to slow down the crystallization process for Sn-based perovskites [21,22]. Furthermore, additives such as tin fluoride (SnF_2), hypophosphorous acid and other reducing vapor atmosphere were introduced during the perovskite fabrication process to reduce the oxidation of Sn^{2+} [18,23–25]. Interfacial engineering to reduce the interfacial recombination rates and promote charge collection efficiency, was also proved to be an effective approach to improve the device performance [26–30]. The state-of-the-art PCE for tin-rich Sn-Pb alloyed perovskite has reached to 19.03% with negligible hysteresis [31]. However, the devices still suffer from low moisture and oxygen stability.

Recently, reduced-dimensional perovskite in which the inorganic PbI_6^{4-} was perpendicular to the substrate facilitated efficient charge transport and led to improved moisture stability [32,33]. Moreover, the inclusion of organic ammonium spacer could help to stabilize bulk perovskite materials to achieve pure perovskite phase [34–37]. Similar strategy to form two-dimensional/three-dimensional (2D/3D) bilayer structure was also demonstrated to be able to improve the hole extraction efficiency and decrease the surface defect, which significantly improved the power conversion efficiency [38–41]. Bearing this in mind, we believe the strategies can be extended to Sn-Pb alloyed perovskites to improve the materials and device stabilities. As documented, the formation of low dimensional perovskite by introducing butylammonium (BA) and phenylethylammonium (PEA) cations into traditional 3D perovskites was utilized to promote devices performance and stability of pure Sn^{2+} based perovskites [19,42,43]. In addition, introducing bulky ammonium functionalize with carbonyl group into the Pb-Sn alloyed perovskite thin film by Lewis acid coordination was utilized to form vertically oriented 2D layered perovskite

achieving excellent stability in ambient condition [44]. Furthermore, high orientated tin perovskite was obtained by employing one step mixing 2D and 3D materials [45,46]. However, the PCE of the tin-lead perovskite is still inferior to 3D lead perovskite. The above-mentioned successful approaches encourage us to employ 2D perovskite layer on surface of the tin-lead perovskite. Herein, we took full advantages of 2D and 3D tin-lead perovskite and fabricated perovskite films by two-step mixing of 2D and 3D materials to obtain devices with excellent performance and moisture stability.

Based on the above, here we introduced a versatile ultrathin 2D perovskite $\text{PEA}_2\text{Pb}_{0.4}\text{Sn}_{0.6}\text{I}_4$ on the top of 3D $(\text{FASnI}_3)_{0.6}-(\text{MAPbI}_3)_{0.4}$ perovskite film to improve their stability. 2D perovskite layer was formed by phenethylammonium iodide (PEAI) *in situ* treatment on fabricated 3D perovskite film. We verified 2D perovskite layer contributed not only to hole extraction with defect healing effect but also enhancing water and oxygen resistance serving as a shielding layer. We fabricated the conventional-structure (n-i-p) photovoltaic devices achieving a maximum power conversion efficiency of 15.5% with negligible hysteresis, maintaining 60% its initial efficiency after 40 h exposure in the ambient condition.

2 Experimental

2.1 Materials and precursor preparation

Perovskite precursors including lead iodide (PbI_2), methylammonium iodide (MAI), formamidinium iodide (FAI), tin iodide (SnI_2), lead thiocyanate ($\text{Pb}(\text{SCN})_2$) and tin fluoride (SnF_2) were purchased from Sigma-Aldrich (USA) (99.99%). TiO_2 was prepared according to literature [47]. Spiro-OMeTAD and PEA were purchased from Xi'an Polymer Light Technology Corp (China) (99.9%). Au and bis(trifluoromethane)sulfonamide lithium (LiTFSI) were purchased from Sigma-Aldrich (USA) (99.99%). Some solvents such as *N,N*-dimethylformamide (DMF), dimethyl sulfoxide (DMSO), toluene (HPLC), chlorobenzene (CB) isopropanol (IPA), acetonitrile (ACN) and 4-*tert*-butylpyridine (TBP) were purchased from Sigma-Aldrich (USA) (anhydrous, 99.8%). The 3D precursor solution, $(\text{FASnI}_3)_{0.6}-(\text{MAPbI}_3)_{0.4}$, was prepared as following. First, the 1.4 M FASnI_3 precursor solution was prepared by dissolving 521 mg of SnI_2 and 240 mg of FAI with 10 mol% (21.9 mg) of SnF_2 in 800 μL DMF and 200 μL DMSO, stirring for 3–6 h at room temperature. Secondly, mixing 159 mg of MAI and 461 mg of PbI_2 with 3.5 mol% (11.3 mg) $\text{Pb}(\text{SCN})_2$ in 630 μL DMF and 70 μL DMSO to obtain 1.4 M MAPbI_3 precursor solution. Finally, the designed precursor solution was obtained by combining stoichiometric amounts of FASnI_3 with MAPbI_3 perovskite precursor solutions. The hole transport material (HTM) solution was prepared as

following. Spiro-OMeTAD (72.3 mg) was dissolved in 1 mL CB with additives of 17.5 μL LiTFSI solution (520 mg in 1 mL ACN) and 28.8 μL TBP. Different concentrations of PEAi solutions were prepared as following. PEAi (20 mg) was dissolved in 1 mL IPA. Then diluting PEAi concentration of 20 mg mL^{-1} can obtain different concentrations of PEAi solutions.

2.2 Perovskite solar cell fabrication

Patterned ITO glass substrates were sequentially cleaned with detergent solution, acetone, and isopropanol. The TiO_2 electron transport layers (ETLs) were spin-coated on ITO substrates from the colloidal TiO_2 nanocrystal solutions, and annealed on a hot plate at the displayed temperature of 150 $^{\circ}\text{C}$ for 30 min in ambient air, according to the reference [47]. Then the substrates were transferred into nitrogen-filled glovebox when cooling at room temperature. The 3D perovskite films were deposited onto the TiO_2 substrates with two sequential spin coating procedures. The first step was 2000 rpm for 10 s with an acceleration of 200 rpm s^{-1} . During the second step of 5000 rpm for 20 s with a ramp-up of 2500 rpm s^{-1} , 400 μL toluene was poured on the substrate at 15 s before the end of the procedure. Then the substrate was transferred on a hotplate and heated at 70 $^{\circ}\text{C}$ for 30 min after leaving at room temperature for 2 min. In order to fabricate additional 2D perovskite layer, we spin-coated 50 μL of PEAi solution dissolved in weak polar isopropanol with different concentrations (0.5, 0.8, 1, 3, 6, 10 mg mL^{-1}) at 6000 rpm for 30 s, and annealed at 100 $^{\circ}\text{C}$ for 10 min. Spiro-OMeTAD solution was subsequently deposited on the perovskite layers at 4000 rpm for 20 s. Finally, the devices were completed by depositing 100 nm of gold electrodes on top of HTM layer using thermal evaporation.

2.3 Photovoltaic device characterization

The current density-voltage (J - V) curves of solar cells were measured with a Keithley 2400 source unit (USA) under simulated illumination AM 1.5G. We calibrated light intensity by employing reference Si solar cell (Newport) with the mismatch factor less than 5%. A mask of area 0.16 cm^2 was utilized in J - V measurement in order to accurately evaluate current density. The devices were measured under forward scan (0–0.8 V, step 0.02 V) or reverse scan (0.8–0 V, step 0.02 V) with no delay time. External quantum efficiency (EQE) spectra were obtained from a QE system (PV Measurements Inc., USA).

2.4 Characterizations and measurements

The samples for X-ray diffraction (XRD) were made by fabricating perovskite films on the glass substrates. XRD

patterns were performed using 40 kV, 40 mA Cu $\text{K}\alpha$ ($\lambda=0.15406$ nm) radiation by Mini Flex 600 (Rigaku, Japan). The ultraviolet (UV) characterization of perovskite films were carried out on a Lambda 950 UV-Vis spectrophotometer (USA). The samples were made by depositing perovskite films on the glass/ TiO_2 substrates. The photoluminescence (PL) spectra were measured with a Fluorolog-Horiba fluorometer (Japan). Time-resolved photoluminescence (TRPL) experiments were performed using an exciting wavelength of 532 nm. The top scanning electron microscope (SEM) images were recorded on JEOL JSM-7500F (Japan) with an accelerating voltage of 1 kV. The cross-section SEM of devices were performed with a FEI Nova dual beam (USA), focused ion beam system, including SEM and gallium ion beam instrument. The X-ray photoelectron spectroscopy (XPS) spectra of perovskite samples were collected by Thermo Scientific ESCALAB 250Xi (USA) with Al $\text{K}\alpha$ radiation source. A reference of C1s (284.8 eV) was calibrated all the binding energies. Ultraviolet photoelectron spectroscopy (UPS) spectra were recorded with an Imaging Photoelectron Spectrometer (Thermo Scientific ESCALAB 2650Xi, USA), with a non-monochromated He I α photon source ($h\nu=21.22$ eV).

3 Results and discussion

The conventional device structure (n-i-p) was employed in this study. As shown in Figure 1(b), the detailed device structure can be expressed as ITO/ TiO_2 /3D perovskite/2D perovskite/Spiro-OMeTAD/Au. 3D perovskite and 2D perovskite stand for $(\text{FASnI}_3)_{0.6}(\text{MAPbI}_3)_{0.4}$ and $\text{PEA}_2\text{Pb}_{0.4}\text{Sn}_{0.6}\text{I}_4$ perovskite. The procedure of fabricating 2D/3D perovskite film includes two steps. The first step is fabricating 3D perovskite film using antisolvent assistant deposition method. The second step is depositing 2D perovskite on top of the 3D perovskite.

This step involves applying different concentration of phenethylammonium iodide (PEAi) isopropanol solution on top of the as-prepared 3D-perovskite film. As shown in Figure 1(a), the representative diffraction peaks for 2D perovskite, $\text{PEA}_2\text{Pb}_{0.4}\text{Sn}_{0.6}\text{I}_4$, located on 5.8 $^{\circ}$, 11.3 $^{\circ}$, 16.7 $^{\circ}$, 22.2 $^{\circ}$, 27.7 $^{\circ}$ and 33.36 $^{\circ}$, as well as 39.11 $^{\circ}$ for 2θ in XRD patterns. When the PEAi concentration is 0.8 mg mL^{-1} , the diffraction peak of the 2D perovskite film at about 5.8 $^{\circ}$ appears and other peaks are unobvious. With increase of PEAi concentration, the intensity of diffraction peaks for 2D perovskite is more and more strong. The enlargement of XRD about $2\theta<10^{\circ}$ of PEAi in different concentrations shows that the intensity of diffraction peaks for 2D perovskite is more and more obvious with increase of PEAi concentration, indicating the formation of 2D perovskite (Figure S1, [Supporting Information online](#)). Moreover, when applying PEAi

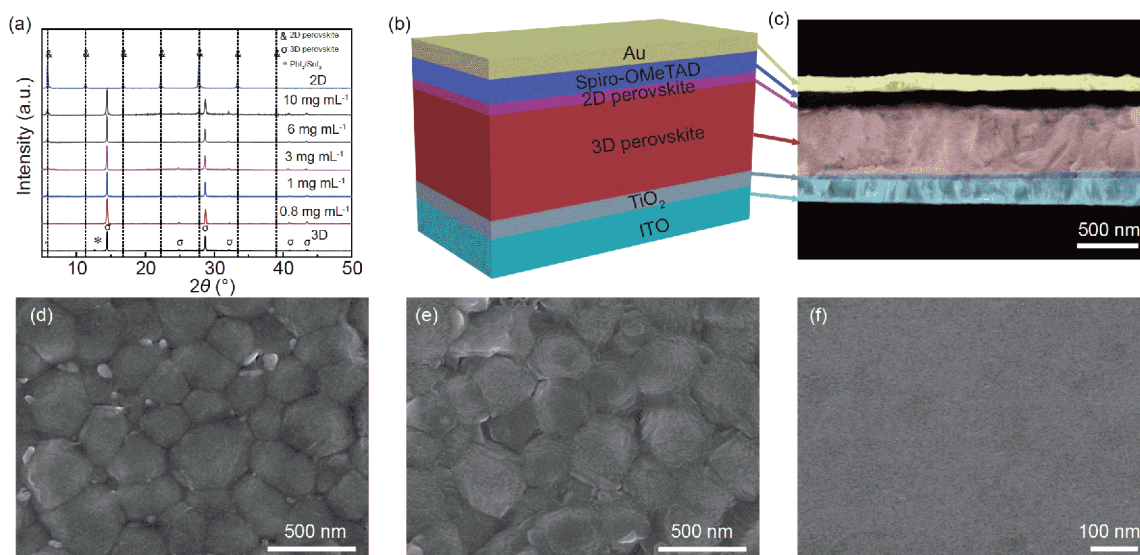


Figure 1 (a) X-ray diffraction pattern of 2D/3D perovskite with different concentrations of PEA solutions, 0.8, 1, 3, 6 and 10 mg mL⁻¹; (b) the conventional device structure (n-i-p) used in the present work; (c) cross-sectional SEM image of 2D/3D devices; top-view SEM images of (d) the 3D perovskite film and (e) the 2D/3D perovskite film and (f) the 2D perovskite film on TiO₂ substrate (color online).

on top of the 3D perovskite with the concentration of 10 mg mL⁻¹, all diffraction peaks shown in XRD spectra can be assigned as the peaks come from 3D perovskite and 2D perovskite. The XRD pattern confirms that 2D perovskite PEA₂Pb_{0.4}Sn_{0.6}I₄ can be formed by applying different concentrations of PEA solution on top of 3D perovskite films. We speculate that a pronounced peak of (FASnI₃)_{0.6}(MAPbI₃)_{0.4} at 12.65° can result from PbI₂/SnI₂ [15]. Possible reaction mechanism speculated is cation exchange. It is that bulk organic ammonium cations infiltrating 3D perovskite partly replace small cation inserting in the corner-sharing tin-lead halide octahedral skeleton and 2D perovskite can generate on the surface of 3D perovskite [48,49]. We prepared the perovskite film of PEA treatment with a thickness of 500 nm as shown in cross-sectional SEM image in Figure 1 (c). And 2D perovskite layer cannot be apparently shown because thickness is too thin. From the top view scanning in Figure 1(d), the original 3D perovskite film is a dense and pinhole-free film with an average grain size of ~500 nm. When the PEA concentration is 0.5 mg mL⁻¹, PbI₂/SnI₂ crystals become small (Figure S2(a)). When the PEA concentration is more than 1 mg mL⁻¹, grain sizes and grain boundaries decrease and deduce. After PEA treatment, PbI₂/SnI₂ crystals situated on the surface of films are reacted and the surface of film become smooth (Figure S2). This is similar to the influence of amine gas post-treatment where perovskite films on surface were dissolved by amine and reformed during annealing process, leading to smooth film [50]. However, increasing content 2D perovskite layer hinders hole extraction from perovskite to Au layer contributing to decreased device performance. And according to XRD and SEM, one of best morphologies can be gained when

PEAI concentration is 1 mg mL⁻¹ (Figure 1(e)). And 2D/3D perovskite films prepared by solution of optimized concentration (1 mg mL⁻¹) were carried out following measurements without specific instruction. In addition, morphology of 2D perovskite film is very smooth without grain (Figure 1(f)). These smooth surface appearances indicate 2D thin layer can be uniform coverage on 3D perovskite layer serving as a protective layer. So the formation of 2D thin layer is utilized to block the moisture and oxygen invasion in 3D perovskite film.

XPS representation is effective to detect surface property of sample. In order to verify the generation of 2D passivation layer, we carried out the XPS measurements on the perovskite films of 3D, 2D, and 2D/3D. Figure 2(a) presents C1s spectrum of 3D detected at binding energy of 284.7 eV (C–H) and 286.2 eV (C–N) for the existence of MA⁺/FA⁺. Besides, in the N1s spectrum of 3D perovskite film (Figure 2 (d)), the binding energy of C–NH₂ bond is at 402.1 eV ascribed to the existence of MA⁺ and the binding energy of C=NH₂⁺ bond is at 400.2 eV owing to the existence of FA⁺. In the Sn 3d XPS spectrum of 3D perovskite layer, the content of Sn⁴⁺ is much higher than the amount of Sn²⁺, which verifies 3D film is vulnerable to the oxidation oxygen (Figure S3(a)). So we speculate the emergence of C=O at binding energy of 288.2 eV may result from oxygen-induced oxidation of the 3D perovskite film. The special bonds of the 2D perovskite film is of π–π (291.5 eV), which is corresponding to the phenyl of featured group about PEA⁺ cation (Figure 2(b)).

As a result, only a typical peak at 402.0 eV for the bond C–NH₂ can be obtained in N1s spectra of 2D thin film (Figure 2 (e)). And for the XPS spectrum of Sn 3d peaks of 2D thin

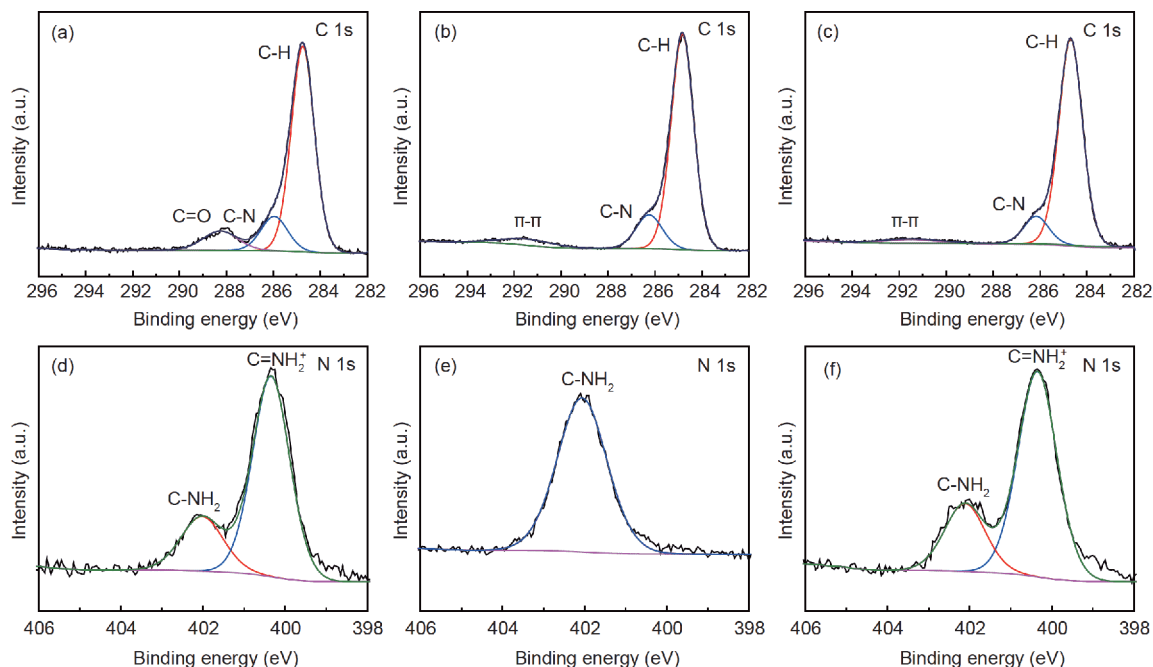


Figure 2 XPS spectra of (a) C1s and (d) N1s of 3D perovskite film; XPS spectra of (b) C1s and (e) N1s of 2D perovskite film; XPS spectra of (c) C1s and (f) N1s of 2D/3D perovskite film (the concentration of PEA is 1 mg mL^{-1}) (color online).

layer (Figure S3(b)), the amount of Sn^{2+} is much higher than the amount of Sn^{4+} . This makes striking contrast with Sn 3d peaks of 3D film, indicating 2D perovskite layer can reduce oxygen invasion in perovskite. The bond of π - π is presented in 2D/3D film (Figure 2(c)) and 2D film. However, this is absent from 3D film. In addition, the emergence of some typical bonds such as C-NH₂ and C=NH₂⁺ in N1s XPS spectrum of the 2D/3D film (Figure 2(f)) also exist in 3D perovskite layer. Above all, this strongly confirms the formation of 2D thin layer. As shown in Figure S3(c), the amount of Sn^{2+} is higher than the amount of Sn^{4+} and the ratio of $\text{Sn}^{2+}/\text{Sn}^{4+}$ of Sn 3d peaks in 2D/3D perovskite film is much more than that of Sn3d peaks of 3D perovskite film. This perfectly confirms that 2D perovskite capping layer can reduce unintentional oxidation of Sn^{2+} . So we reach a conclusion from XPS results that 2D $\text{PEA}_2\text{Pb}_{0.4}\text{Sn}_{0.6}\text{I}_4$ passivation layer is situated on the surface of 3D perovskite and can protect the tin-lead halide perovskite from oxygen damage.

To reveal the effect of 2D perovskite layer on fabricated 2D/3D PSCs, UPS was employed to detect the bandgap of the 3D and 2D/3D perovskite film. For 3D control and 2D/3D, cut-off of binding energies ($E_{\text{cut-off}}$) are 16.85 and 16.90 eV, respectively, as illustrated in Table S1 (Supporting Information online). In Figure 3(a), work functions (W_f) of 3D, 2D/3D perovskite film are calculated to be 4.37 and 4.32 eV, and using the formula of $W_f = 21.22 - E_{\text{cut-off}}$, respectively [51]. In Figure 3(b), the value of $E_F - E_V$ decreases from 1.15 to 1.05 eV where E_F and E_V stand for Fermi level and valence band maximum, revealing that E_V is much closer to E_F after PEA treatment. The E_V (−5.52 eV) of 3D film is

lower than the E_V (−5.37 eV) of 2D/3D film, indicating the cover of 2D perovskite layer can reduce Sn^{2+} oxidation [52]. In Figure S4(a), the bandgap (E_g) of films 3D, 2D/3D, 2D are calculated to be 1.26, 1.26 and 1.96 eV according to the formula of $E_g = 1240/\lambda_{\text{edge}}$ (band edge). Consequently, the conduction band minimum $E_C = E_V + E_g$ of 3D, 2D/3D films are −4.26 and −4.11 eV, respectively. And cut-off binding energy of film 2D is 16.88 eV in Figure S4(b). In Figure S4 (c), $E_F - E_V$ of film 2D is 1.00 eV. E_V and E_C of film 2D are calculated to be −5.34 and −3.38 eV. The energy level diagram of devices can be obtained in Figure 3(c), where E_C and E_V of films 3D and 2D/3D are measured while those of Spiro-OMeTAD and TiO_2 are used from Ref. [6]. With energy level increased grading, the edge of valence band maximum and the edge of conduction band minimum ascending gradient facilitate a graded hole channel, efficiently pushing hole transfer from perovskite to HTM and creating additional energy obstacle that prevent back electron shift from perovskite to HTM. 3D perovskite films on surface produced by a regular solution process have been reported to be defective. However, some interfacial transport materials were found to reduce and decrease charge recombination rates [53,54]. We speculate that 2D perovskite may reduce defects and trap states and converse the surface defect of 3D perovskite into 2D perovskite. To confirm effect of 2D interface layer suppressed nonradiative recombination, time-resolved photoluminescence (TRPL) measurements were performed on without and with PEA treatment films. First, the samples on glass substrates were carried out steady-state photoluminescence (PL). After PEA treatment, the 2D/3D

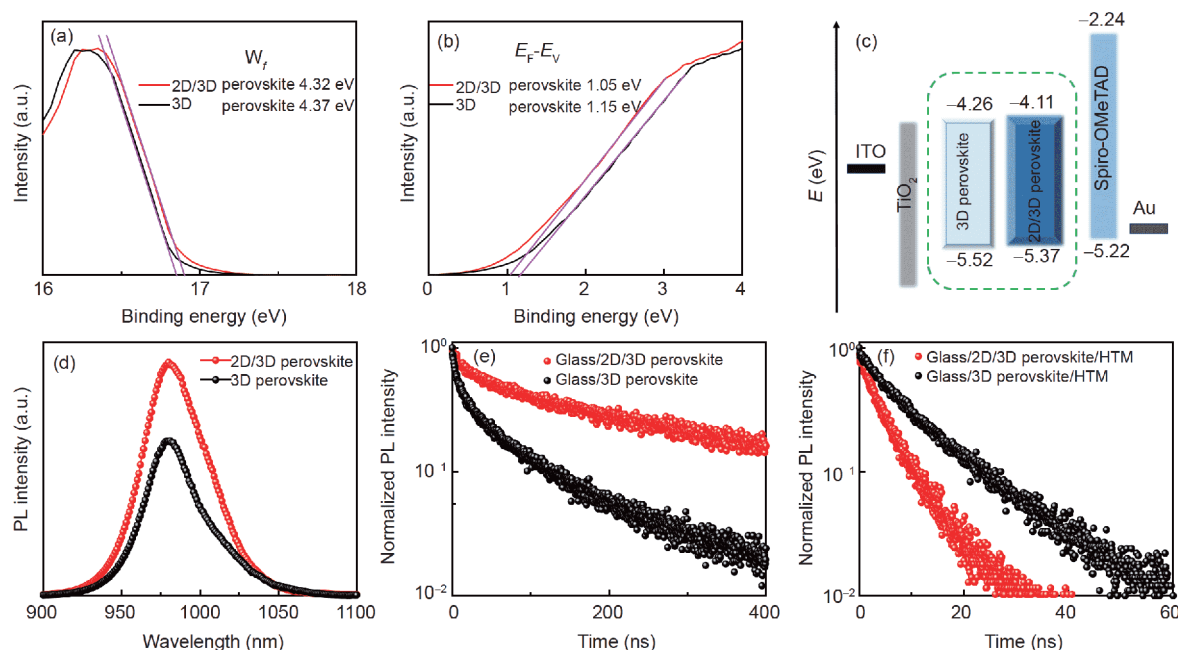


Figure 3 UPS spectra of 3D and 2D/3D perovskite film. (a) The work function (W_f) of 3D and 2D/3D perovskite films; (b) E_F-E_V binding energy of 3D and 2D/3D perovskite films; (c) the energy-level diagram of device; (d) steady-state PL spectra of glass/3D and 2D/3D perovskite films; (e) the time-resolved PL decay curves of the glass/3D and 2D/3D perovskite films; (f) the time-resolved PL decay curves of the glass/3D perovskite/HTM and 2D/3D perovskite/HTM (color online).

film had a stronger PL intensity and the PL emission of 2D/3D film did not show obvious shift compared with 3D control (Figure 3(d)). This enhanced PL intensity may ascribe to reduced surface traps by 2D passivation layer. In Figure 3(e), PL lifetime of 3D films is 98.71 ns, and after PEAi modification, the carrier lifetime enhances to 348.08 ns shown in Table S2. TRPL spectra revealed increased PL lifetime for 2D/3D films. This phenomenon indicates the decreased surface recombination defects and trap states via PEAi treatment. Also we took space charge limited current measurements on 2D/3D (1 mg mL⁻¹) and 3D perovskite film. The hole trap-state density for the 3D and 2D/3D perovskite films are calculated to be 5.86×10^{15} and 2.54×10^{15} cm⁻³, respectively (Figure S5). The reduced trap-state density results from PEA treatment, indicating that the formation of the 2D perovskite layer can passivate surface and grain boundaries trap [48,55]. Further to clarify the influence of 2D perovskite layer on the hole transport dynamics between interface, TRPL measurements were carried out samples whose structure is glass/perovskite films/HTM. When 3D and 2D/3D perovskite films were formed on HTM, carrier lifetimes sharply decreased in Figure 3(f). More importantly, the film 2D/3D with HTM represents enhanced charge extraction compared with the film 3D. This further suggested that the formation of 2D perovskite layer can not only reduce surface recombination sites but also effectively promote charge transport. This can well account for the improved open-circuit voltage (V_{oc}) and negligible hysteresis in devices 2D/3D.

We also took the $J-V$ measurements on fabricated 3D and PEAi treatment devices. Device performance and stability can be improved and enhanced by PEAi modification optimizing the concentration of the solution (Figure 4(a)). Changing PEAi concentration from 0 to 1 mg mL⁻¹, devices performance significantly improves and the champion device can be obtained with 1 mg mL⁻¹ PEAi treatment. The best devices with efficiency of 15.5% and V_{oc} of 0.77 V, short circuit current density (J_{sc}) of 26.60 mA cm⁻² and fill factor (FF) of 75.67% can be achieved. This may attribute to 2D thin layer that can increase charge transfer and reduce the rates of surface recombination with the resistance to oxygen damage. However, we observed a significant drop in performance for 2D/3D perovskite devices when the concentration of PEAi solution is high than 1 mg mL⁻¹. With the increase of PEAi concentration, V_{oc} keep about 0.74 V, FF reduce from 0.75 to 0.71 but J_{sc} highly decrease from 26.60 to 24.72 mA cm⁻². A reason can be explained that increasing content of 2D perovskite layer can effectively block back electron shift as revealed by significantly preserved V_{oc} while it hinders hole extraction from perovskite to Au layer contributing to decreased J_{sc} and FF. Further, $J-V$ curves of the 3D devices and optimized PEAi treatment devices are measured under different scans. The 2D/3D devices showed lower hysteresis in contrast with large hysteresis about 3D PSCs (Figure 4(b, c)). Figure 4(d) represents EQE spectra of devices and curves of integrated J under the AM 1.5G solar spectrum. The value of the integrated J from EQE spectra for 2D/3D reaches 26.60 and 23.16 mA cm⁻² about 3D PSCs. In

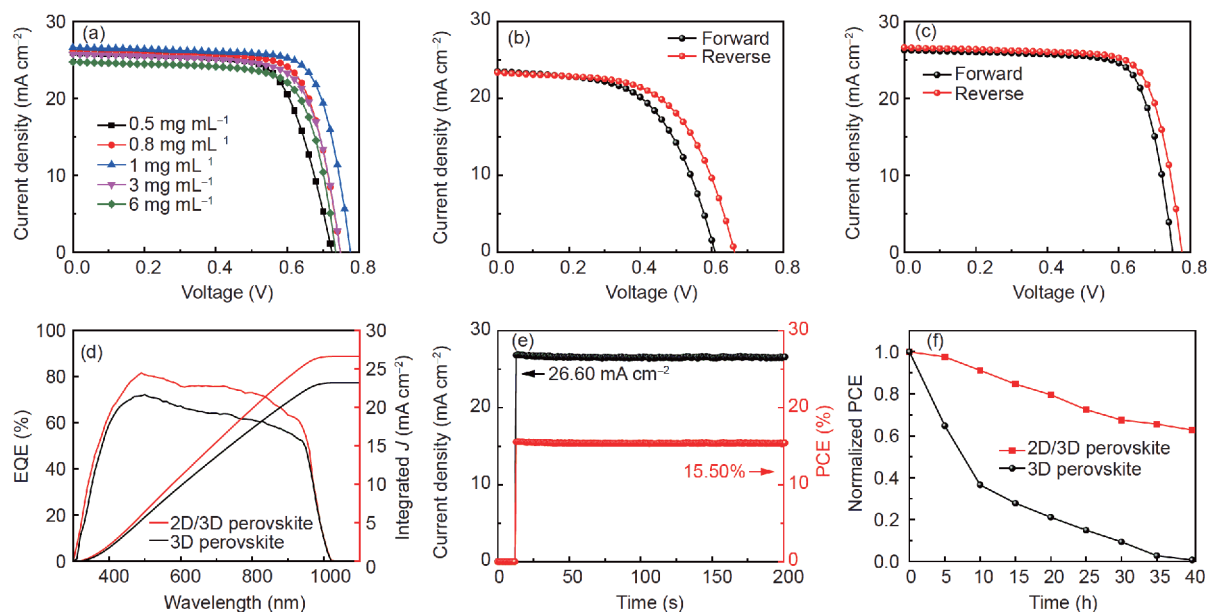


Figure 4 *J*-*V* curves of (a) 2D/3D perovskite solar cells using PEAi solutions with concentrations of 0.5, 0.8, 1, 3 and 6 mg mL⁻¹ under reverse scans, (b) 3D perovskite solar cell and (c) 2D/3D champion perovskite solar cell; (d) the corresponding EQE spectra of 3D and 2D/3D PSCs under AM 1.5G 1 sun illumination and the integrated *J* of the fabricated 3D PSCs and 2D/3D PSCs; (e) stabilized photocurrent measurement at the maximum power point (0.58 V) of 2D/3D PSCs; (f) the long-term stability of normalized PCE of the fabricated 3D and 2D/3D PSCs storing in the ambient condition with RH 30%±10% (color online).

Figure 4(e), to verify the reproducibility of our devices, we independently tested steady-state current density and PCE at voltage according to maximum output power ($V_{\max}=0.58$ V). The photocurrent densities of those increase sharply to maximum over several seconds and then keep balance at ~ 26.60 mA cm⁻², leading to the stabilized PCE of 15.50%, which agrees well with *J*-*V* curves tested in reverse scan. In addition, the stability of PSCs is a key factor on their commercial application. We tracked device stability in the N₂-filled glovebox without encapsulation under continuous illumination. 2D/3D device preserved 60% of its initial efficiency while 3D device dropped to 20% of its initial efficiency after 400 h (Figure S6). The enhanced stability can be attributed to improved crystallinity and surface passivation by 2D capping layer, leading to high resistance to light illumination and strengthened stability. Moreover, we investigated the long-term stability of devices with and without PEAi modification in relative humidity (RH) 30%±10% air environment. 3D devices completely failed while 2D/3D devices maintained 60% its initial efficiency after 40 h exposure to air (Figure 4(f)). The devices of other parameter variations showed in Figure S7. The devices of PEAi modification exhibit enhanced stability as compared with reference 3D. Film stability tests in air condition with RH 30%±10% were carried out to comprehend discrepancy about 3D and 2D/3D devices (Figure S8). 3D samples experienced fast degradation in air condition while 2D/3D samples did not show obvious decomposition until after 40 h

stored in air condition. These tests agree well with the result of devices stability.

4 Conclusions

In conclusion, we have demonstrated high efficient, and moisture-stable PSCs with no hysteresis by employing 2D perovskite capping layer PEA₂Pb_{0.4}Sn_{0.6}I₄ on the top of 3D (FASnI₃)_{0.6}(MAPbI₃)_{0.4} perovskite film. 2D perovskite layer reduces surface recombination and increases hole extraction between interfacial layers. Together with enhanced oxygen resistance and moisture stability in 2D/3D PSCs as compared to 3D PSCs, a record of 15.5% in tin-lead perovskites solar cells is achieved in our work. The devices of 2D/3D display improved stability and retain 60% its initial efficiency after 40 h exposure in air condition. This work provides an effective method to improve the oxygen resistance and moisture stability for lead-tin iodide PSCs.

Acknowledgements This work was supported by the National Natural Science Foundation of China (21771114), MOE 111 (B12015), the Natural Science Foundation of Tianjin (17JCYBJC40900, 18YFZCGX00580), and the Fundamental Research Funds for the Central Universities. M. Yuan thanks to the financial support from “Thousand Youth Talents Plan of China”.

Conflict of interest The authors declare that they have no conflict of interest.

Supporting information The supporting information is available online at <http://chem.scichina.com> and <http://link.springer.com/journal/11426>. The

supporting materials are published as submitted, without typesetting or editing. The responsibility for scientific accuracy and content remains entirely with the authors.

- 1 Zhang W, Eperon GE, Snaith HJ. *Nat Energy*, 2016, 1: 16048
- 2 Yang WS, Park BW, Jung EH, Jeon NJ, Kim YC, Lee DU, Shin SS, Seo J, Kim EK, Noh JH, Seok SI. *Science*, 2017, 356: 1376–1379
- 3 Hu Y, Zhang Z, Mei A, Jiang Y, Hou X, Wang Q, Du K, Rong Y, Zhou Y, Xu G, Han H. *Adv Mater*, 2018, 30: 1705786
- 4 Arora N, Dar MI, Hinderhofer A, Pellet N, Schreiber F, Zakeeruddin SM, Grätzel M. *Science*, 2017, 358: 768–771
- 5 Kojima A, Teshima K, Shirai Y, Miyasaka T. *J Am Chem Soc*, 2009, 131: 6050–6051
- 6 Jeon NJ, Na H, Jung EH, Yang TY, Lee YG, Kim G, Shin HW, Il Seok S, Lee J, Seo J. *Nat Energy*, 2018, 3: 682–689
- 7 Hao F, Stoumpos CC, Cao DH, Chang RPH, Kanatzidis MG. *Nat Photon*, 2017, 8: 489–494
- 8 Stoumpos CC, Frazer L, Clark DJ, Kim YS, Rhim SH, Freeman AJ, Ketterson JB, Jang JI, Kanatzidis MG. *J Am Chem Soc*, 2015, 137: 6804–6819
- 9 Slavney AH, Hu T, Lindenberg AM, Karunadasa HI. *J Am Chem Soc*, 2016, 138: 2138–2141
- 10 Saparov B, Hong F, Sun JP, Duan HS, Meng W, Cameron S, Hill IG, Yan Y, Mitzi DB. *Chem Mater*, 2015, 27: 5622–5632
- 11 Cortecchia D, Dewi HA, Yin J, Bruno A, Chen S, Baikie T, Boix PP, Grätzel M, Mhaisalkar S, Soci C, Mathews N. *Inorg Chem*, 2016, 55: 1044–1052
- 12 Ju MG, Chen M, Zhou Y, Garces HF, Dai J, Ma L, Padture NP, Zeng XC. *ACS Energy Lett*, 2018, 3: 297–304
- 13 Liao W, Zhao D, Yu Y, Shrestha N, Ghimire K, Grice CR, Wang C, Xiao Y, Cimaroli AJ, Ellingson RJ, Podraza NJ, Zhu K, Xiong RG, Yan Y. *J Am Chem Soc*, 2016, 138: 12360–12363
- 14 Hao F, Stoumpos CC, Chang RPH, Kanatzidis MG. *J Am Chem Soc*, 2015, 137: 8094–8099
- 15 Li Y, Sun W, Yan W, Ye S, Rao H, Peng H, Zhao Z, Bian Z, Liu Z, Zhou H, Huang C. *Adv Energy Mater*, 2016, 6: 1601353
- 16 Zhao D, Yu Y, Wang C, Liao W, Shrestha N, Grice CR, Cimaroli AJ, Guan L, Ellingson RJ, Zhu K, Zhao X, Xiong RG, Yan Y. *Nat Energy*, 2017, 2: 17018
- 17 Koh TM, Krishnamoorthy T, Yantara N, Shi C, Leong WL, Boix PP, Grimsdale AC, Mhaisalkar SG, Mathews N. *J Mater Chem A*, 2015, 3: 14996–15000
- 18 Song TB, Yokoyama T, Stoumpos CC, Logsdon J, Cao DH, Wasielewski MR, Aramaki S, Kanatzidis MG. *J Am Chem Soc*, 2017, 139: 836–842
- 19 Shao S, Liu J, Portale G, Fang HH, Blake GR, ten Brink GH, Koster LJA, Loi MA. *Adv Energy Mater*, 2018, 8: 1702019
- 20 Wang N, Zhou Y, Ju MG, Garces HF, Ding T, Pang S, Zeng XC, Padture NP, Sun XW. *Adv Energy Mater*, 2016, 6: 1601130
- 21 Liao W, Zhao D, Yu Y, Grice CR, Wang C, Cimaroli AJ, Schulz P, Meng W, Zhu K, Xiong RG, Yan Y. *Adv Mater*, 2016, 28: 9333–9340
- 22 Hao F, Stoumpos CC, Guo P, Zhou N, Marks TJ, Chang RPH, Kanatzidis MG. *J Am Chem Soc*, 2015, 137: 11445–11452
- 23 Lee SJ, Shin SS, Kim YC, Kim D, Ahn TK, Noh JH, Seo J, Seok SI. *J Am Chem Soc*, 2016, 138: 3974–3977
- 24 Stoumpos CC, Malliakas CD, Kanatzidis MG. *Inorg Chem*, 2013, 52: 9019–9038
- 25 Kayesh ME, Chowdhury TH, Matsuishi K, Kaneko R, Kazaoui S, Lee JJ, Noda T, Islam A. *ACS Energy Lett*, 2018, 3: 1584–1589
- 26 Ke W, Stoumpos CC, Logsdon J, Wasielewski MR, Yan Y, Fang G, Kanatzidis MG. *J Am Chem Soc*, 2016, 138: 14998–15003
- 27 Ke W, Priyanka P, Vegiraju S, Stoumpos CC, Spanopoulos I, Soe CMM, Marks TJ, Chen MC, Kanatzidis MG. *J Am Chem Soc*, 2018, 140: 388–393
- 28 Kapil G, Ripolles TS, Hamada K, Ogomi Y, Bessho T, Kinoshita T, Chantana J, Yoshino K, Shen Q, Toyoda T, Minemoto T, Murakami TN, Segawa H, Hayase S. *Nano Lett*, 2018, 18: 3600–3607
- 29 Ran C, Xi J, Gao W, Yuan F, Lei T, Jiao B, Hou X, Wu Z. *ACS Energy Lett*, 2018, 3: 713–721
- 30 Xu G, Bi P, Wang S, Xue R, Zhang J, Chen H, Chen W, Hao X, Li Y, Li Y. *Adv Funct Mater*, 2018, 28: 1804427
- 31 Li C, Song Z, Zhao D, Xiao C, Subedi B, Shrestha N, Junda MM, Wang C, Jiang CS, Al-Jassim M, Ellingson RJ, Podraza NJ, Zhu K, Yan Y. *Adv Energy Mater*, 2019, 9: 1803135
- 32 Jiang Y, Yuan J, Ni Y, Yang J, Wang Y, Jiu T, Yuan M, Chen J. *Joule*, 2018, 2: 1356–1368
- 33 Quan LN, Yuan M, Comin R, Voznyy O, Beauregard EM, Hoogland S, Buin A, Kirmani AR, Zhao K, Amassian A, Kim DH, Sargent EH. *J Am Chem Soc*, 2016, 138: 2649–2655
- 34 Zhang X, Ren X, Liu B, Munir R, Zhu X, Yang D, Li J, Liu Y, Smilgies DM, Li R, Yang Z, Niu T, Wang X, Amassian A, Zhao K, Liu SF. *Energy Environ Sci*, 2017, 10: 2095–2102
- 35 Yang R, Li R, Cao Y, Wei Y, Miao Y, Tan WL, Jiao X, Chen H, Zhang L, Chen Q, Zhang H, Zou W, Wang Y, Yang M, Yi C, Wang N, Gao F, McNeill CR, Qin T, Wang J, Huang W. *Adv Mater*, 2018, 30: 1804771
- 36 Zhang T, Dar MI, Li G, Xu F, Guo N, Grätzel M, Zhao Y. *Sci Adv*, 2017, 3: e1700841
- 37 Wang Z, Lin Q, Chmiel FP, Sakai N, Herz LM, Snaith HJ. *Nat Energy*, 2017, 2: 17135
- 38 Grancini G, Roldán-Carmona C, Zimmermann I, Mosconi E, Lee X, Martineau D, Nabey S, Oswald F, De Angelis F, Graetzel M, Nazeeeruddin MK. *Nat Commun*, 2017, 8: 15684
- 39 Chen P, Bai Y, Wang S, Lyu M, Yun JH, Wang L. *Adv Funct Mater*, 2018, 28: 1706923
- 40 Chen J, Seo JY, Park NG. *Adv Energy Mater*, 2018, 8: 1702714
- 41 Hu Y, Qiu T, Bai F, Ruan W, Zhang S. *Adv Energy Mater*, 2018, 8: 1703620
- 42 Cao DH, Stoumpos CC, Farha OK, Hupp JT, Kanatzidis MG. *J Am Chem Soc*, 2015, 137: 7843–7850
- 43 Liao Y, Liu H, Zhou W, Yang D, Shang Y, Shi Z, Li B, Jiang X, Zhang L, Quan LN, Quintero-Bermudez R, Sutherland BR, Mi Q, Sargent EH, Ning Z. *J Am Chem Soc*, 2017, 139: 6693–6699
- 44 Chen Z, Liu M, Li Z, Shi T, Yang Y, Yip HL, Cao Y. *iScience*, 2018, 9: 337–346
- 45 Ramirez D, Schutt K, Wang Z, Pearson AJ, Ruggeri E, Snaith HJ, Stranks SD, Jaramillo F. *ACS Energy Lett*, 2018, 3: 2246–2251
- 46 Wang F, Jiang X, Chen H, Shang Y, Liu H, Wei J, Zhou W, He H, Liu W, Ning Z. *Joule*, 2018, 2: 2732–2743
- 47 Tan H, Jain A, Voznyy O, Lan X, Garcia de Arquer FP, Fan JZ, Quintero-Bermudez R, Yuan M, Zhang B, Zhao Y, Fan F, Li P, Quan LN, Zhao Y, Lu ZH, Yang Z, Hoogland S, Sargent EH. *Science*, 2017, 355: 722–726
- 48 Lin Y, Bai Y, Fang Y, Chen Z, Yang S, Zheng X, Tang S, Liu Y, Zhao J, Huang J. *J Phys Chem Lett*, 2018, 9: 654–658
- 49 Chen Y, Yu S, Sun Y, Liang Z. *J Phys Chem Lett*, 2018, 9: 2627–2631
- 50 Zhou Z, Wang Z, Zhou Y, Pang S, Wang D, Xu H, Liu Z, Padture NP, Cui G. *Angew Chem Int Ed*, 2015, 54: 9705–9709
- 51 Park M, Kim JY, Son HJ, Lee CH, Jang SS, Ko MJ. *Nano Energy*, 2016, 26: 208–215
- 52 Yang Z, Rajagopal A, Chueh CC, Jo SB, Liu B, Zhao T, Jen AKY. *Adv Mater*, 2016, 28: 8990–8997
- 53 Shao Y, Xiao Z, Bi C, Yuan Y, Huang J. *Nat Commun*, 2014, 5: 5784
- 54 Fang Y, Bi C, Wang D, Huang J. *ACS Energy Lett*, 2017, 2: 782–794
- 55 Li P, Zhang Y, Liang C, Xing G, Liu X, Li F, Liu X, Hu X, Shao G, Song Y. *Adv Mater*, 2018, 30: 1805323